# BOREAL-A Fixed-Wing Unmanned Aerial System for the Measurement of Wind and Turbulence in the Atmospheric Boundary Layer

Sara Alaoui-Sosse, Pierre Durand, Patrice Medina, Philippe Pastor, Michel Gavart, Sergio Pizziol

# BOREAL—A Fixed-Wing Unmanned Aerial System for the Measurement of Wind and Turbulence in the Atmospheric Boundary Layer

SARA ALAOUI-SOSSE,[a,b] PIERRE DURAND,[b] PATRICE MEDINA,[b] PHILIPPE PASTOR,[a] MICHEL GAVART,[c] AND SERGIO PIZZIOL[c]

[a] *ISAE-SUPAERO, Université de Toulouse, Toulouse, France*
[b] *Laboratoire d'Aérologie, Université de Toulouse, CNRS, UPS, Toulouse, France*
[c] *BOREAL SAS, Castanet-Tolosan, France*

(Manuscript received 17 September 2021, in final form 13 December 2021)

ABSTRACT: An instrumentation package for wind and turbulence observations in the atmospheric boundary layer on an unmanned aerial vehicle (UAV) called BOREAL has been developed. BOREAL is a fixed-wing UAV built by BOREAL company, which weighs up to 25 kg (5 kg of payload) and has a wingspan of 4.2 m. With a light payload and optimal weather conditions, it has a flight endurance of 9 h. The instrumental payload was designed in order to measure every parameter required for the computation of the three wind components, at a rate of 100 $s^{-1}$, which is fast enough to capture turbulence fluctuations: a GPS–inertial measurement unit (IMU) platform measures the three components of the groundspeed a well as the attitude angles; the airplane nose has been replaced by a five-hole probe in order to measure the angles of attack and sideslip, according to the so-called radome technique. This probe was calibrated using computational fluid dynamics (CFD) simulations and wind tunnel tests. The remaining instruments are a Pitot tube for static and dynamic pressure measurement and temperature/humidity sensors in dedicated housings. The optimal airspeed at which the vibrations are significantly reduced to an acceptable level was defined from qualification flights. With appropriate flight patterns, the reliability of the mean wind estimates, through self-consistency and comparison with observations performed at 60 m on an instrumented tower could be assessed. Promising first observations of turbulence up to frequencies around 10 Hz and corresponding to a spatial resolution to the order of 3 m are hereby presented.

KEYWORDS: Atmosphere; Boundary layer; Turbulence; Aircraft observations; Europe

## 1. Introduction

Over the past few decades, the development of remotely piloted aircraft systems (RPASs) has played a crucial role in atmospheric observations, allowing researchers to measure atmosphere parameters such as wind vectors, temperature, and humidity, with high accuracy and resolution. The flying part of an RPAS is known as an unmanned aerial vehicle (UAV). It can cover a wide space range and areas that are unreachable with instrumented piloted airplanes, radiosondes, and masts/towers. UAVs can nowadays also embark sophisticated systems taking advantage of the miniaturization of electronic devices.

Elston et al. (2015) classified fixed-wing UAVs according to three main categories, depending on their weight, endurance, and payload capacities. UAVs weighing between 10 and 30 kg represent the first category; they are characterized by a high endurance (between 4 and 40 h) and high payload capacity but they are very expensive and often difficult to operate. In this category, Application of Light-weight Aircraft for Detecting In situ Aerosol (ALADINA) UAV (25 kg and 3.6-m wing span) developed to measure atmospheric particles, solar radiation, wind components up to a frequency of around 7 Hz, and temperature up to 25 Hz may be mentioned (Bärfuss et al. 2018; Altstädter et al. 2015).

Manta is a runway takeoff and landing UAV of 27.7 kg able to measure radiative as well as latent and sensible heat fluxes in terrestrial and marine atmospheric boundary layer (ABL) (Reineman et al. 2013). The Boeing ScanEagle is capable of ship based launch and recovery and weighs 22 kg. Wind components and humidity were measured up to 25 Hz (1.3-m horizontal resolution) and temperature up to 5 Hz (6.6-m horizontal resolution) (Reineman et al. 2013).

The second category includes UAVs that weigh more than 1 kg and less than 10 kg. In this category, the $M^2AV$, which has a wingspan of 2 m and weighs 6 kg may be taken into account. This system is able to measure wind fluctuations up to 40 Hz, which is equivalent to a spatial resolution of 55 cm at an airspeed of 22 m $s^{-1}$ (van den Kroonenberg et al. 2008). The Multi-Purpose Airborne Sensor Carrier (MASC) (5–7.5 kg) and its newest version MASC-3 both proved their capacity to measure turbulence up to 30 Hz (0.6-m resolution) at 19.7 m $s^{-1}$ (Wildmann et al. 2014a; Rautenberg et al. 2019). Rautenberg et al. (2018) compared the two commonly used algorithms for wind retrieval (Pitot tube algorithm and no-flow sensor algorithm) with the wind vector measured by the five-hole probe. BLUECAT5 (5 kg) has a payload that measures turbulence with a sampling rate of 60 Hz corresponding to 0.28 m of spatial resolution at 17 m $s^{-1}$ (Witte et al. 2017). The Small Multifunction Autonomous Research and Teaching Sonde (SMARTSonde) (3.5 kg, 1.7-m wingspan) was developed in order to measure profiles of the meteorological variables and heat fluxes, as well as to indirectly determine the wind from navigation parameters (Bonin et al. 2013a,b). In addition,

*Corresponding author*: Sara Alaoui-Sosse, sara.alaoui-sosse@isae-supaero.fr, sara.alaoui-sosse@aero.obs-mip.fr

DOI: 10.1175/JTECH-D-21-0126.1

our team has developed Objet Volant Leger Instrumenté–Turbulence Atmosphérique (OVLI-TA), a UAV of 3.5 kg and a 2.6-m wingspan; this was operated to measure mean profiles in the ABL as well as turbulence up to 10 Hz at 13 m $s^{-1}$ (Alaoui-Sosse et al. 2019). The Tempest (3.2 kg and 6.8-m wingspan) was designed at the University of Colorado Boulder in order to sample pretornadic and tornadic supercell thunderstorms (Elston 2011). The Collaborative Colorado–Nebraska NexSTAR weighs 5 kg, has a wingspan of 1.7 m and was developed to collect observations of temperature, moisture, pressure, and wind velocity (Houston et al. 2012).

In the last category (UAVs weighing less than 1 kg), we should mention the small unmanned meteorological observer (SUMO) (Reuder et al. 2009), capabilities and limitations of which are described by Reuder et al. (2016) and Båserud et al. (2016). The DataHawk (0.7 kg and 0.9-m wingspan) is capable of wind measurements with a 40-m horizontal resolution and a 4-m vertical resolution (Lawrence and Balsley 2013). Such UAVs have restricted endurance and payload capacity, but are easily deployable to carry out small experiments with less cost.

The scientific payloads on UAVs for ABL studies are designed to measure at least some of the following parameters: wind, temperature, moisture, atmospheric composition, and turbulence. The wind and its turbulent fluctuation are two of the more complex parameters to measure. The wind is generally computed as the sum of the ground speed and airspeed vectors. This last parameter is heavier to obtain on multirotor type UAVs, because the rotor wash effect distorts the flows around the platform. This difficulty could be bypassed by installing a sonic anemometer on a mast high enough above the platform (Barbieri et al. 2019). Here the study has focused on the fixed-wing UAV type. Furthermore, the remote sensing capabilities of UAVs have not been discussed, but the measurements in the ABL with a focus on wind and turbulence have been concentrated on.

The wind vector estimate requires measurement/computation of the ground speed, the attitude angles, and the airspeed vector (see details in section 2b below), at a rate compatible with the desired resolution. Such techniques were used for a long time onboard instrumented piloted airplanes and were significantly improved by the use of the Kalman filter on the inertial platforms. Inertial measurement units (IMUs) are now available at a size/weight small/light enough to be embedded even onboard small UAVs, together with performances compatible with the required accuracy. The true airspeed vector is in general obtained from a multihole probe, which is either installed at the tip of a boom ahead of the airplane, or on the (possibly modified) nose of the airplane following the principle first developed by Brown et al. (1983). A large majority of UAVs have the probe mounted on a boom, though in the past numerous piloted aircraft have been equipped with a radome since Brown et al.'s pioneering work. Such radomes were either the original nose of the aircraft, or a nose specifically designed to reproduce the shape of a hemisphere, hence ensuring calibration coefficients close to the corresponding well-known theoretical values. Examples of such aircraft can be found in, e.g., Tjernström and Friehe (1991), Lambert and Durand (1998), Saïd et al. (2005, 2010), or Raga and Abarca (2007). On UAVs, however, the radome solution is much more original. It was implemented with OVLI-TA (Alaoui-Sosse et al. 2019) as well as with BOREAL, the UAV presented in this paper.

Different calibration and validation procedures have been set up. Wind tunnel tests allow the determination of the coefficients relying on the differential pressures measured on the multihole probe for airspeed and angles of attack and sideslip (Alaoui-Sosse et al. 2019; Calmer et al. 2018). Flight maneuvers, such as back and forth runs, are used to evaluate the consistence of the mean wind estimates (Lenschow 1986a), and (possibly) to adjust some coefficients to take into account, e.g., a misalignment between IMU and aerodynamic frames resulting from successive mounting/dismounting operations of the payload. Spectral analysis reveals the quality of turbulence parameters, the wind components being expected to follow the Kolmogorov's $-5/3$ power law in the inertial subrange. Possible nonperfectly compensated vibrational movements of the platform could also be detected through this way. The required upper frequency to achieve satisfactory turbulence observations varies according to flight level and the airspeed of the UAV: on one hand, turbulence relevant scales decrease when approaching the surface, which requires a finer sampling; on the other hand, the faster the airspeed, the higher the sampling rate required for a given spatial resolution.

When possible, the parameters computed from UAV observations are compared to other platforms used as a reference. During the Lower Atmospheric Process Studies at Elevation—A Remotely piloted Aircraft Team Experiment (LAPSE-RATE) campaign, observations of temperature, humidity, pressure, wind speed, and wind direction performed on 38 (fixed-wing and multirotor) UAVs were analyzed by Barbieri et al. (2019) and compared to those of a meteorological tower used as a reference. Such operations are valuable for establishing the more appropriate sensor installations, such as a proper aspiration and radiation shielding for temperature and moisture measurements. Profiles in the ABL of wind, temperature, and humidity obtained with the OVLI-TA platform were compared to radiosonde observations. In addition, the observed differences between ascending and descending profiles were utilized to estimate the time response of temperature and humidity measurement devices (Alaoui-Sosse et al. 2019). Three GPS-based wind-retrieval algorithms were evaluated in comparison with rawinsonde and sodar data by Bonin et al. (2013b). SUMO wind and turbulence spectra obtained during several flights of the Boundary-Layer Late Afternoon and Sunset Turbulence (BLLAST) campaign were successfully compared to those computed from a sonic anemometer installed at 60 m on a tower by Reuder et al. (2016). It was demonstrated that the OVLI-TA system was able to capture, during a 1-h flight in the vicinity of the same tower, the mean wind and its evolution as well as the turbulent fluctuations up to frequencies of around 10 Hz (Alaoui-Sosse et al. 2019).

A valuable contribution to the ABL observation brought by piloted airplanes was the estimate of kinematic fluxes of

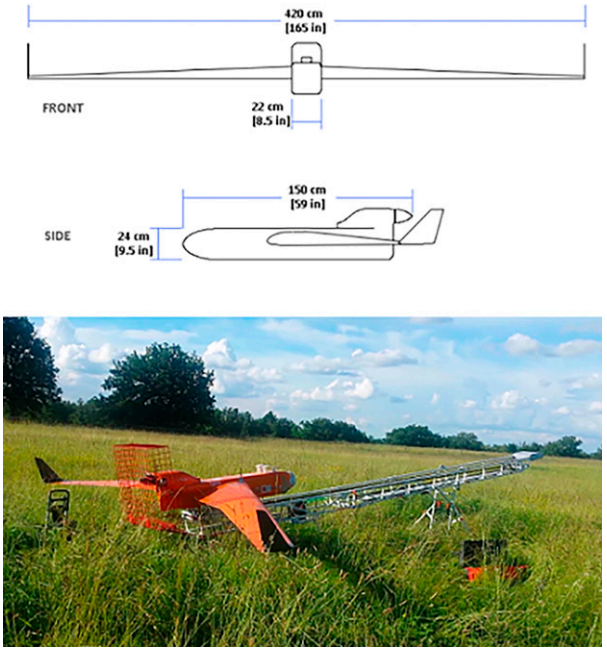


FIG. 1. (top) Geometrical characteristics of the BOREAL UAV. (bottom) The BOREAL installed on the catapult before takeoff.

heat and momentum. Given the size of turbulence scales in the ABL, such estimates require long straight and level runs (i.e., >10 km) to be statistically significant (Mann and Lenschow 1994; Brilouet et al. 2017). Such runs are not easy to operate with UAVs, even with high endurance platforms, mainly due to air traffic restrictions. Excepting over open seas, it is often impossible—at least over populated areas—to fly for distances longer than $O(1)$ km. The uncertainties on eddy-covariance (EC) estimates over such short distances proving unacceptable, alternate methods were set up, based, for example, on heat budget equation in order to estimate the kinematic heat flux, and validated against EC estimates performed on piloted instrumented aircraft (Båserud et al. 2020).

In this paper the development of an instrumental payload for wind and turbulence measurements in the atmospheric boundary layer on board the so-called BOREAL fixed-wing UAV is presented. This development was performed by the Laboratoire d'Aérologie in Toulouse (France). The 20-kg BOREAL platform has the capacity to embark 5 kg of payload, and to fly up to 10 h even in turbulent conditions.

The paper is organized as follows: In section 2, the technical characteristics of BOREAL UAV, the instrumentation developed for turbulence measurements as well as the acquisition system are presented. The calibrations of the five-hole probe through computational fluid dynamics (CFD) simulations as well as wind tunnel tests are then highlighted in section 3. In section 4 the results of experimental flights, from which the optimal flight configuration is deduced is then presented, followed by the results of the wind speed, wind direction estimates, the spectra of wind components, and the comparison with the 60-m tower observations. Conclusions are presented in section 5.

## 2. BOREAL instrumentation

### a. Airframe characteristics

The BOREAL UAV (Fig. 1) is constructed by the eponymous manufacturer (www.boreal-uas.com) and owned by the MISTRAL group. It has a wingspan of 4.20 m and a fuselage length of 1.5 m. It is powered by an internal gasoline engine; its cruise speed varies between 20 and 36 m $s^{-1}$ and its maximum speed is 50 m $s^{-1}$. The flight ceiling is 4500 m. This UAV weighs up to 25 kg depending on the payload mass and fuel quantity, and can embark 5 kg of payload. Its operation can take advantage from its high endurance that can reach 10 h of flight. It embarks an in-house built autopilot and a navigation system that includes a radar altimeter. Takeoff is operated by a catapult. The characteristics of BOREAL are summarized in Table 1.

### b. Wind vector estimation

To estimate the wind vector, multiple parameters are required and need to be measured appropriately and accurately. The wind ($\mathbf{V}_w$, air motion relative to Earth) is the sum of the air motion with respect to the aircraft called the airspeed ($\mathbf{V}_{\text{air}}$) and the aircraft motion relative to Earth known as the ground speed ($\mathbf{V}_g$):

$$\mathbf{V}_w = \mathbf{V}_g + \mathbf{V}_{\text{air}}. \tag{1}$$

A GPS-IMU coupled system gives us the ground speed components: $U_g$, $V_g$, and $W_g$ according to the respective east, north, and upward vertical directions.

The airspeed is computed from the dynamic pressure measured in our system by the five-hole probe and a Pitot tube as explained in the next section. Given that the airspeed of BOREAL is around 30 m $s^{-1}$, it can be assumed that the flow

TABLE 1. Technical characteristics of the BOREAL.

| Fuselage length | Dry weight | Maximum speed | Ascent speed range |
|---|---|---|---|
| 1.5 m | 20 kg | 50 m $s^{-1}$ | 5–10 m $s^{-1}$ |
| Wingspan | Max payload | Cruise speed | Endurance, flight ceiling |
| 4.2 m | 5 kg | 20–36 m $s^{-1}$ | 8–10 h, 4500 m |

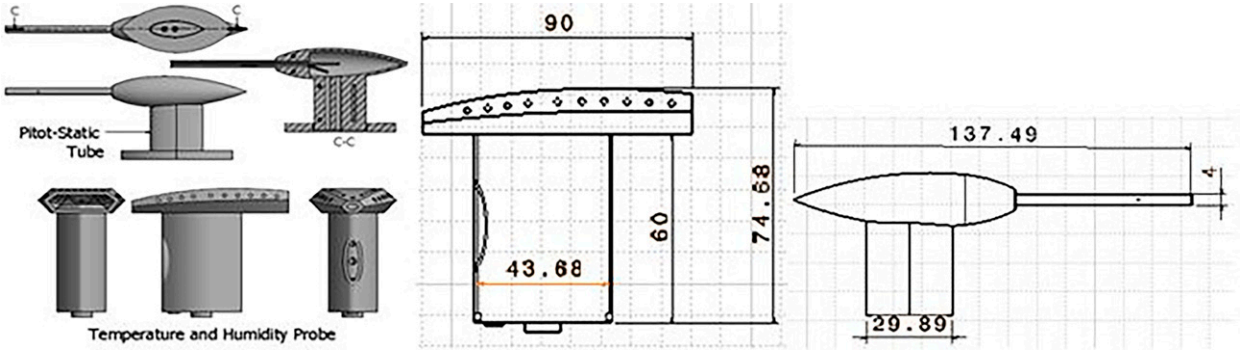


FIG. 2. Different views of the Pitot tube and the temperature/moisture housings and their dimensions (in mm).

is incompressible. The Bernoulli equation to estimate the velocity of the airflow can thereby be used:

$$V_a = \|\mathbf{V}_{\text{air}}\| = \sqrt{\frac{2P_{\text{dyn}}}{\rho}}\ , \tag{2}$$

where $\rho$ is the density of the air that is calculated from the perfect gas law and $P_{\text{dyn}}$ is the dynamic pressure that is the differential pressure (total minus static); the effects of humidity were neglected.

As stated by Lenschow (1986a), the wind components with respect to the Earth referential are expressed as

$$U = -V_a D^{-1}[\sin\psi\cos\theta + \tan\beta\,(\cos\psi\cos\phi + \sin\psi\sin\theta\sin\phi) + \tan\alpha\,(\sin\psi\sin\theta\cos\phi - \cos\psi\sin\phi)] + U_g, \tag{3}$$

$$V = -V_a D^{-1}[\sin\psi\cos\theta + \tan\beta\,(\cos\psi\cos\phi + \sin\psi\sin\theta\sin\phi) + \tan\alpha\,(\sin\psi\sin\theta\cos\phi - \cos\psi\sin\phi)] + V_g, \tag{4}$$

$$W = -V_a D^{-1}[\sin\theta - \tan\beta\cos\theta\sin\phi - \tan\alpha\cos\theta\cos\phi] + W_g, \tag{5}$$

where $U$, $V$, and $W$ are the three components of the wind vector pointing toward east, north, and vertical upward, respectively; $\psi$ is the true heading; $\phi$ is the roll angle; $\theta$ is the pitch angle; $\alpha$ is the angle of attack and $\beta$ is the angle of sideslip (they are measured by the five-hole probe ;see next paragraph); and $D$ is defined as $D = (1 + \tan^2\alpha + \tan^2\beta)^{1/2}$.

The sign conventions are those used in aeronautics, and when all the angles are small, simplified formulations for the above equations can be used (Lenschow 1986b; Alaoui-Sosse et al. 2019).

### c. *Instrumentation of BOREAL*

The instrumental payload was defined in order to measure all the parameters present in the above equations. Temperature and moisture are relevant parameters for ABL studies as well as for the computation of air density. Two identical temperature and humidity sensors SHT75 were placed in dedicated housings (Fig. 2), the advantages of which are a shielding against a spurious elevation of temperature under the effect of solar radiation, and prevention from probe wetting by droplets. Such housings were already used and characterized by Alaoui-Sosse et al. (2019) and are placed in the front and top of BOREAL fuselage (as shown in Figs. 1 and 8). The SHT75 sensors are designed by the company Sensirion. They provide digital output and simultaneously measure both temperature and relative humidity with an accuracy of ±0.3°C and ±1.8%, respectively. A Pitot tube installed along the fuselage provides static pressure, as well as the dynamic pressure from which the airflow velocity ($V_a$) can be computed [Eq. (2)].

To calculate the angles of attack and sideslip, we replaced the nose of the BOREAL with a 3D printed, hemispherical five-hole probe (Fig. 3). There are five pressure ports: the center hole is in the longitudinal axis of the airplane, the four others are placed above and below and to the right and left of the central hole, making an angle of 45° to the center of the

FIG. 3. Picture (front view) of the five-hole probe mounted on BOREAL.

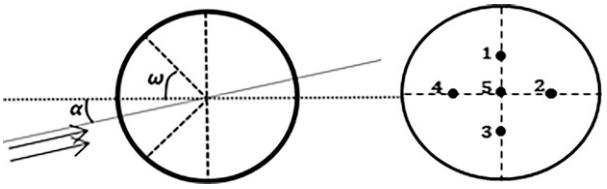


FIG. 4. Scheme of a five-hole spherical probe; (left) side view for an angle of attack $\alpha$; (right) front view with the holes numbers.

sphere. The diameter of the hemisphere and holes is 18.4 cm and 1 mm, respectively.

The equation relating the measured pressure and the angle of attack $\alpha$ is provided by Brown et al. (1983):

$$\Delta\hat{P}_\alpha = \hat{P}_1 - \hat{P}_3 = \frac{-9}{4}\sin(2\omega)\sin(2\alpha), \tag{6}$$

where $\hat{P}_1$ and $\hat{P}_3$ are the pressures at the holes above and below the central hole, respectively, normalized by the dynamic pressure, and $\omega$ is the angle between the longitudinal axis of the five-hole probe and the axis passing through one port and the center of the sphere (Fig. 4). Replacing $\alpha$ with $\beta$ and ports 1 and 3 with ports 4 and 2, corresponding to the starboard and larboard holes, respectively, provides the equation for the angle of the sideslip angle. By assuming low values for the angles of attack and sideslip therefore and given that $\omega = -\pi/4$, Eq. (6) can be rewritten as

$$\alpha = k_\alpha^{-1}\Delta\hat{P}_\alpha; \quad \beta = k_\beta^{-1}\Delta\hat{P}_\beta \tag{7}$$

with a theoretical value of $k_\alpha = k_\beta = 4.5\ \text{rad}^{-1}(0.0785\ \text{deg}^{-1})$. In the following section, numerical simulations and wind tunnel tests, which show how the BOREAL probe departs from these values, will be discussed.

In addition to the angles of attack and sideslip, a redundant estimate of $V_a$ can also be obtained with the radome from the differential pressure between the central hole and the static port of the Pitot tube.

The pressure ports on the five-hole probe and the Pitot tube are connected to digital differential pressure transducers through silicone tubes, which have an internal diameter of 2 mm and lengths of 7 and 20 cm, respectively. Two types of transducers developed by the company First Sensor and which are working with distinct principles were used: the first one is the pressure sensor HCEM050 (operating pressure ±50 hPa, accuracy ±0.5 hPa) functioning with a membrane, which provides an analog output, and the second one is an LDE sensor (operating pressure ±5 hPa, accuracy ±0.05 hPa), which is based on thermal flow measurement of gas through a microflow channel integrated within the sensor chip. All sensors are read digitally even if all pressure transducers have an analog output. Each pair of HCEM050 sensors is mounted head to tail (Fig. 5), which allows for the compensation of the acceleration effect on the membranes underlined by, for example, Wildmann et al. (2014b), and thus the reduction of the impact of UAV vibrations on the turbulence measurements. The LDE sensor proved to be less sensitive to the UAV vibrations than the HCEM sensor and was a preferred choice for the computation of the angles of attack and sideslip.

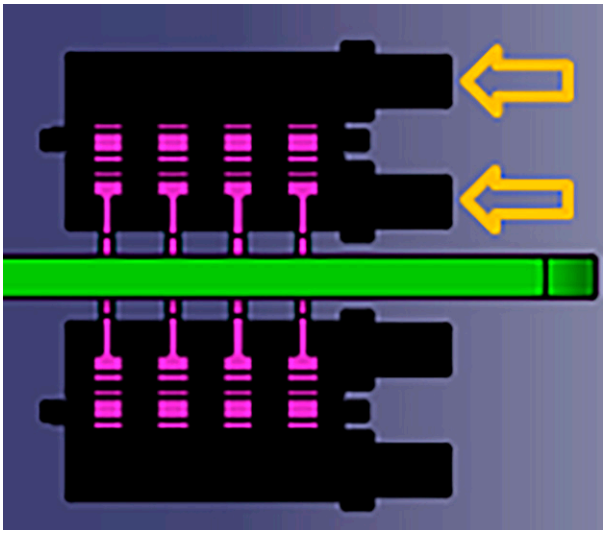

FIG. 5. Pressure sensors (in black) mounted "head to tail" and fixed with the purple pins on both sides of the electronic card (in green).The two air inlets of each sensor are indicated by the arrows.

Two LDEs measure the differential pressures between the upper and lower ports, and between the left and right ports, respectively. Two pairs of HCEM050 are used for dynamic pressure measurements. In each case, the static pressure port is that of the Pitot tube, whereas the total pressure port is either the Pitot head or the central hole of the nose. Table 2 summarizes pressure, temperature, and humidity sensors belonging to the instrumental package. Their manufacturer references are mentioned in addition to their resolution, accuracy, operating range, full scale span, and the time response.

A miniature global navigation satellite system (GNSS)/inertial navigation system (INS) and Altitude and Heading Reference System (AHRS) system (the "Spatial" device from Advanced Navigation) provides pitch, yaw, and roll as well as accelerations. This system is coupled to an Air Data Unit (from the same company) with two pneumatic inlets connected to the Pitot tube static and dynamic pressure ports, respectively. The Air Data Unit, through its own pressure transducers, is thus able to provide redundant estimates of static pressure and true airspeed.

The data acquisition of all parameters (pressures, airspeed, angles of attack and sideslip, attitude angles, three ground speed components, and temperature/humidity) is made at 100 Hz.

To house all electronic components, specific boxes that integrate Pmod connectors (Pmod stands for "peripheral module" interface and is an open standard defined by Digilent Inc. for peripherals used with FPGA) were designed as shown in Fig. 6. These boxes are 3D printed with acrylonitrile butadiene styrene (ABS) material.

### *d. Acquisition system for turbulence measurements*

The electronic system mounted on BOREAL UAV is composed of the FPGA module, which is a Ztex 2.13 FPGA board

TABLE 2. The sensors, their manufacturer, resolution, operating range, full span scale, and response time.

| Parameter | Sensor/manufacturer | Resolution | Accuracy | Operating range/FSS[a] | Response time |
|---|---|---|---|---|---|
| Static pressure | HCE0611/First sensor | 14 bit | ±1%FSS = ±5 hPa | 600 to 1100 hPa/500 hPa | 1 ms |
| Differential pressure | HCEM050/First sensor | 14 bit | ±0.5%FSS = ±0.5 hPa | ±50 hPa/100 hPa | 1 ms |
| Differential pressure | LDE/First sensor | — | ±0.5%FSS = ±0.05 hPa | ±5 hPa/10 hPa | 5 ms |
| Relative humidity | SHT75/Sensirion | 14 bit | ± 1.8% | 0% to 100% | 5–30 s |
| Temperature | SHT75/Sensirion | 12 bit | ± 0.3°C | −40° to 123°C | 8 s |

[a] Full scale span (FSS) is the algebraic difference between the output signal for the highest and lowest specified pressure. Example: for HCEM050 50 − (−50) = 100 hPa.

with Artix-7 XC7A100T and 100 general purpose I/O's (GPIO) connected to FPGA "pinout," in addition to the distributed functional modules (pressure module and MicroSD module). Note that FPGA stands for "field programmable gate arrays," an integrated circuit reconfigured to meet the desired objectives. This type of architecture has several advantages, among these the facility to distribute electronics weight in the UAV, the ease of maintenance during experimentation and the ability to adapt the position of electronics near the five-hole probe. Figures 6 and 7 illustrate the distinct electronic modules and their connections.

First, the central FPGA module is based with an adapter board with the Ztex board and 12 Lemo connectors. Eleven Lemo connectors have 12 pins, 10 of them are for signal and 2 for power supply (GND, 3.3 or 5.5 V); the last Lemo

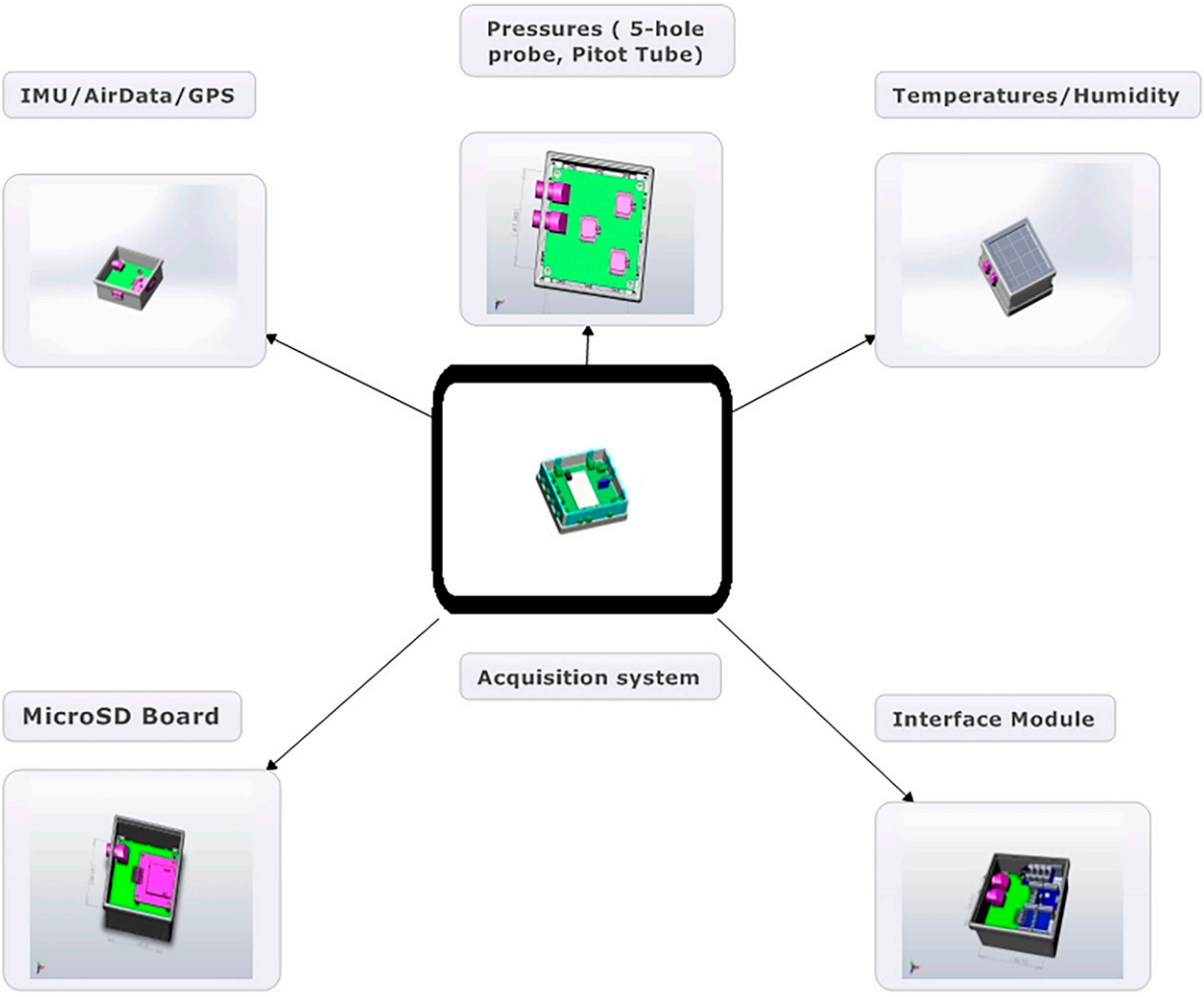


FIG. 6. The acquisition system mounted inside their specific boxes.

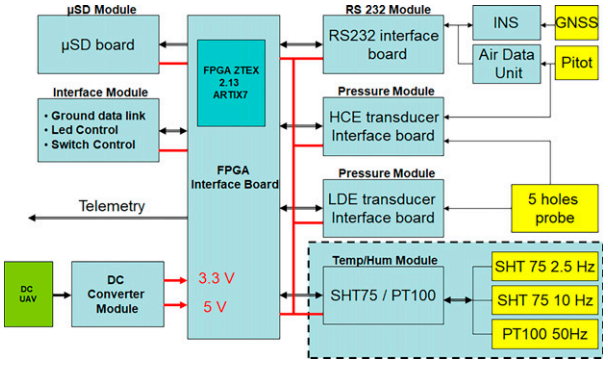


FIG. 7. The acquisition system.

connector has 4 pins and is used to ensure the connection with the mobile data link modem.

The first pressure module is designed for the five-hole probe measurements and it includes the LDE pressure transducers; the second pressure module is composed of HCE pressure sensors to measure airspeed and static pressure.

The "RS232 module" is used to interface three sensors (Rx, Tx, GPIO), the output signal of which follows the RS232 protocol. It is used for interface with the IMU Spatial and the Air Data Unit (ADU). The GPS pulse per second (PPS) impulsion is sent to the FPGA module via this module.

In addition, the "MicroSD module" is used to carry and protect the SD PCB support (SD means Secure Digital and PCB is printed circuit board, which mechanically supports and electrically connects electrical and electronic components).

The "temperature/humidity module" is used for the interface of two sensors of temperature/humidity and a fast temperature sensor PT100 or PT 1000.

Finally, the "interface module" is used for testing and for the setup of the acquisition system. All the data sensors are available through the USB interface (ground data link). All data are sent every second. This module is only used to check electronics before flight tests and is disconnected during flights. All measured data are saved at 100 Hz on the micro-SD ($\mu$SD) board for further postprocessing analysis.

The clock is synchronized with the GPS PPS pulse. Every sensor has its own software management with a local watchdog ensuring a correct recording of data on the $\mu$SD card. The SD control firmware writes the sensors data in an array of 1024 bytes. To control the data acquisition, the telemetry only works if the SD writing system operates well. After flights, the $\mu$SD card can be replaced with a new one, or reused preserving the old data.

### *e. Software description*

The embedded software uses the VHDL code. VHDL means Very High Description Language, which is a hardware description language used in electronic design automation to describe digital and mixed-signal systems such as FPGA used in our system. The code architecture is divided into two parts. First, the Sensor Management module was adapted to each sensor: Each sensor has its own software. This code has first to manage the configuration and initialization, then the readout protocol and interface when necessary (TopReadout). Next is the data backup time to be read before the new readout, and finally the security of the readout cycle. In case of no activity or correct readout of a sensor a new initialization is performed.

Second, the global management module is in charge of transferring data from sensors to $\mu$SD and to an external link. The FPGA global clock is used, and pulses to start the conversion are synchronized with the GPS PPS. Depending on the acquisition frequency needed for each sensor, a top clock signal is generated to start the data readout of the sensor. When the data are ready, they are memorized in a block memory at a specific address.

During the flight, there is a radio link between the autopilot of the airplane and the ground station. This link is used for the control and command of the airplane operation, and can be utilized to real-time adjustments of the scheduled flight plan. Through this link, a subsample of the recorded parameters is also transmitted, in order to check whether the scientific payload works properly, and to allow a first glance at the observations.

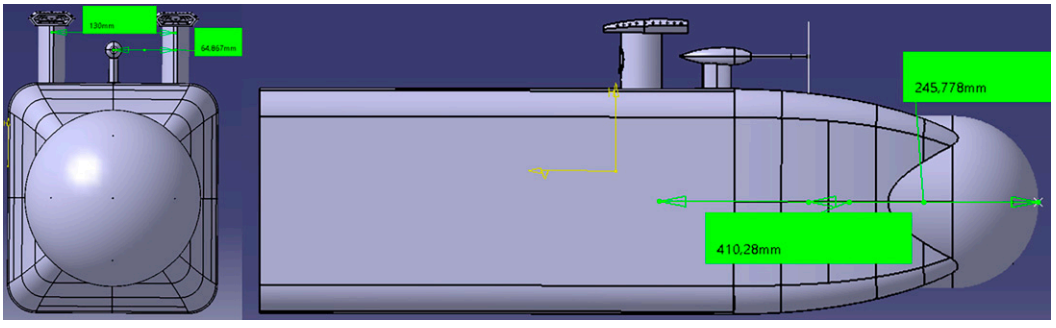


FIG. 8. BOREAL geometry used for CFD simulation. (left) In the front view, the distance between the two housings (130 mm) and between one housing and the Pitot tube (65 mm) is shown. (right) In the side view, the distance between the nose of the UAV and, respectively, the extremity of the Pitot tube (245 mm) and the housings (410 mm) is shown.

## 3. Five-hole probe calibrations

The values of $k_\alpha$ and $k_\beta$ defined above can differ from the theoretical value of 4.5 $\text{rad}^{-1}$ (0.0785 $\text{deg}^{-1}$). This could be due to a nonperfect hemispherical shape of the nose, a shift in the position of the holes with respect to the theoretical position, or a pressure perturbation related to the fine shape of the pressure ports. To estimate the exact value of these coefficients, we relied on numerical simulations and wind tunnel tests.

### *a. CAO and CFD description*

In this section, we present the CFD simulation of BOREAL. We used Ansys Fluent software to simulate the pressure field around the surface of our UAV. The design of the five-hole probe nose started from the numerical model used by the manufacturer to build the airplane. The geometry of the five-hole probe and its mechanical connection to the fuselage was designed from CFD simulations, in order to obtain a pressure field around the nose close to the theoretical shape (flow around a hemispherical body). The corresponding CAD file was then directly transferred to a 3D printer, which means that the CAD for the CFD simulations presented in this paper is strictly identical to the real aircraft geometry.

The geometry used during CFD simulations was simplified in order to reduce the computation time; hence we only meshed the fuselage with the five-hole probe, the temperature/humidity housings and the Pitot probe, without the wings (Fig. 8). The size of the simulation domain is 16 m along the fuselage, and 8 m on the transversal directions. These dimensions have been chosen so that the walls are far enough from the UAV. The simulated flow is incompressible since we flew at 30 m $\text{s}^{-1}$, which means a Mach number lower than 0.3. The boundary condition applied to the borders of the fluid domain is a slip wall with zero shear. A no-slip boundary condition was applied to BOREAL surfaces. A zero pressure outlet boundary condition was fixed.

A tetrahedral meshing was performed with ANSYS to model the flow correctly and to ensure the convergence of the simulation. The UAV surfaces were meshed with a resolution of 1 mm, and a body of 7.2 m along the fuselage axis, and 3 m on the transverse directions was created to refine the mesh around the body of interest (see Fig. 9).

The gravitational acceleration of 9.81 m $\text{s}^{-2}$ was considered. A pressure-based solver was used. The semi-implicit method for pressure linked equations (SIMPLE) algorithm was considered to obtain the pressure field and the method of least squares based on the cells was chosen for gradients and derivatives evaluation. A second-order discretization scheme was used for all equations. The underrelaxation factors were set to 0.2 for pressure, 0.5 for the momentum, turbulent kinetic energy, and turbulent dissipation rate and 1 for density, body forces, and turbulent viscosity; these values are essential for convergence.

Finally, the turbulence model used is the realizable $k$–$\varepsilon$, which contains a different formulation of the turbulent viscosity and a new transport equation for the dissipation rate $\varepsilon$. The density was considered to be constant and equal to 1.225 kg $\text{m}^{-3}$, in addition the operating pressure was set to 101 325 Pa.

In literature, numerical simulations were often reported as a tool to calibrate the probes. For instance, Milanovic and Kalkhoran (2000) and Campbell and Brandon (2011) used CFD simulations together with wind tunnel tests to calibrate

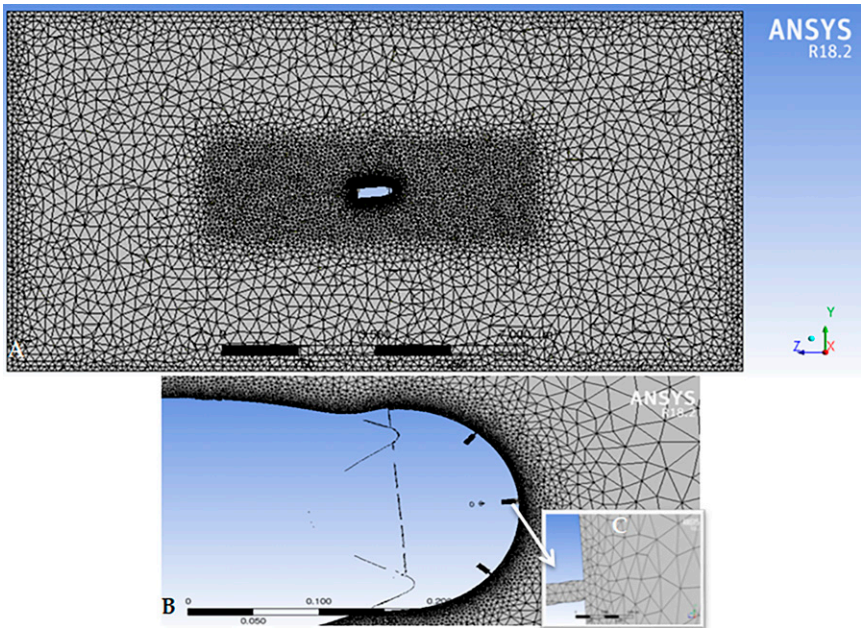


FIG. 9. Illustration of the meshing at $\alpha = 5°$: (a) meshing of the global volume highlighting the refinement around the UAV. (b) Zoom on the meshing around the nose with (c) an inset to expand the vicinity of one of the five holes.

pressure probes. The aim of the simulations performed is to validate the conception design of the five-hole probe, and to numerically estimate the sensitivity factors of this probe [the $k_\alpha$ and $k_\beta$ coefficients in (7)]. For this reason five simulations were run in Ansys Fluent for the angle of attack values of $\{-10°, -5°, 0°, 5°, 10°\}$. Similarly, five simulations were run to estimate the sensitivity factor of the angle of sideslip for the same range of values. For each of the two series, either the angle of attack or the angle of sideslip was set to zero. This range of values was chosen because for an airspeed of 30 m s$^{-1}$ (which is approximately that of the BOREAL), an attack or sideslip angle value of $\pm 10°$ would correspond to a vertical or lateral wind gust of around $\pm 5.2$ m s$^{-1}$, values that are only exceptionally observed in the atmospheric boundary layer. During the flights analyzed later in this paper, we observed attack and sideslip angles values that were always lower than 3° (in absolute value).

As explained in a further section, wind tunnel tests were realized at an airflow speed of 12 m s$^{-1}$. We thus decided to launch a series of numerical simulations at this airflow speed, in order to obtain a set of coefficients directly comparable to those obtained from the wind tunnel tests. Such a comparison gives us a direct evaluation of the configuration used for the numerical simulation, regarding the meshing of the UAV, the noninclusion of the wings, the parameterization of the Ansys Fluent code, etc. A complementary series of simulations was performed at this airflow speed, with the angle of sideslip varying between −10° and +10°, while maintaining the angle of attack at +5°. This test was performed in order to check the possible impact of an angle on each calibration. Similarly, the simulations of the angles of attack and sideslip using this time the airspeed of BOREAL during the flight tests (30 m s$^{-1}$) were launched, in order to evaluate the impact of airflow speed on the five-hole probe calibrations. Eventually, in order to investigate the effect of wings on the simulations results, a simulation including wings was performed. Since it is computationally very expensive, only one configuration was simulated ($\alpha = -5°$, $\beta = 0°$, and the airspeed at 30 m s$^{-1}$). The pressures were extracted at the holes of the probe and then compared to those of the simulation in the same configuration but without the wings. Coherence between the two simulations has been demonstrated, which justifies not using wings during numerical simulations (Table 3).

TABLE 3. Comparison between pressures (deviation from the static pressure of the flow) extracted at the two attack (P1 and P3) and sideslip (P2 and P4) holes of the probe from simulations with and without wings at $\alpha = -5°$ at 30 m s$^{-1}$.

| | P1 (Pa) | P2 (Pa) | P3 (Pa) | P4 (Pa) |
|---|---|---|---|---|
| With wings | 164.9 | 33.0 | −68.8 | 31.3 |
| Without wings | 166.5 | 34.7 | −67.4 | 34.5 |

All of these simulations were run on the supercomputer of Institut Supérieur de l'Aéronautique et de l'Espace (ISAE-SUPAERO). To illustrate the simulation results, three examples of the pressure distribution on the five-hole probe are presented in Fig. 10 for simulations at $\alpha = 5°$ and $\beta = 0°$ (Fig. 10a), at $\alpha = 0°$ and $\beta = 5°$ (Fig. 10b), and at $\alpha = 5°$ and $\beta = 5°$ (Fig. 10c).

### b. Wind tunnel test

The calibration of the five-hole probe was conducted in the wind tunnel at Institut de Mécanique des Fluides de Toulouse (IMFT; in Toulouse, France). The section of the tunnel is 2.4 m × 2.0 m and the theoretical range of flow speed produced is from 1 to 30 m s$^{-1}$, but during this test the flow speed was limited to 12 m s$^{-1}$, because of the constraints imposed by the structure that lifts the heavy UAV. Figure 11 shows the BOREAL during the wind tunnel test.

Different tests were conducted during which the BOREAL was fixed onto a structure allowing the modification and control of its pitch angle. During this calibration procedure, it is considered that when the roll angle is zero in the wind tunnel flow, the pitch of the structure and the angle of attack must be identical; in the same manner after rolling the UAV by 90°, the pitch of the structure will be equal to the angle of sideslip.

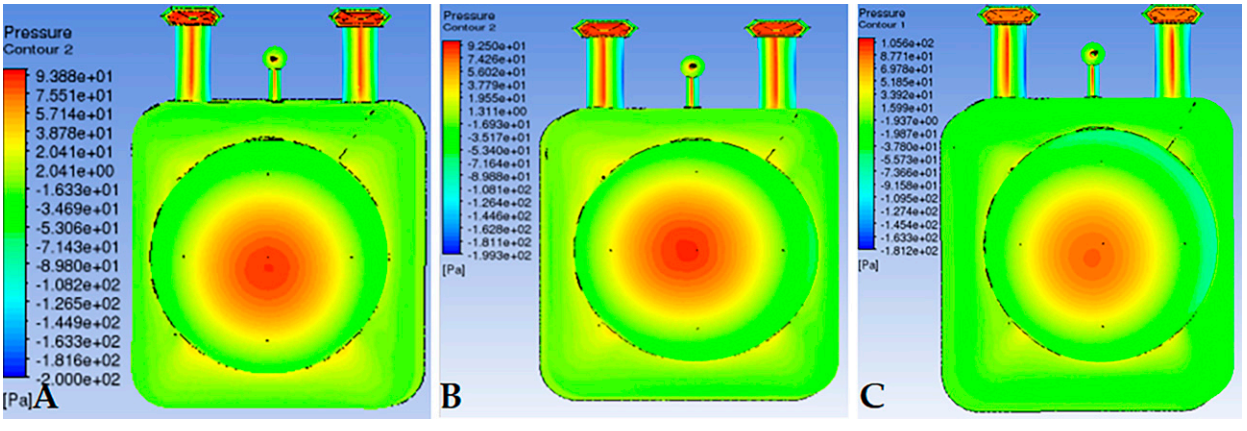


FIG. 10. Simulation of the pressure variation (in Pa) on the body (front view) for (a) $\alpha = 5°$ and $\beta = 0°$, (b) $\alpha = 0°$ and $\beta = 5°$, (c) $\alpha = 5°$ and $\beta = 5°$.

FIG. 11. BOREAL in the wind tunnel test at IMFT.

The first wind tunnel test was performed with the flow speed and pitch angle set at zero to test the data acquisition system and to check the offset value of the IMU pitch. Afterward, the angles were varied between −10° and +10°, for a flow speed of 12 m s$^{-1}$.

### c. Calibration results

The values of $k_\alpha$ and $k_\beta$ were estimated with a least mean square regression on Eq. (7), from both numerical simulations and the wind tunnel test. Bernoulli's equation was used to estimate the dynamic pressure from the airflow velocity in order to normalize the differential pressures between the upper and lower ports ($P_1$ and $P_3$) and between the right and left ports ($P_4$ and $P_2$).

Table 4 shows the results obtained from the numerical simulations at 12 and 30 m s$^{-1}$ for the angles of attack and sideslip, as well as those from the wind tunnel test. For each coefficient, we indicated the value of the determination coefficient of the regression ($R^2$).

First of all, we have to mention that $R^2$ values are always higher than 0.99, which translates as there being no scatter in the regression that might be invoked to explain uncertainties in the coefficients. We then note that $k_\alpha$ and $k_\beta$ values differ (by around 5%–10%) from the theoretical value (0.0785 deg$^{-1}$). Such differences justify a tight calibration process.

We also observe a very good agreement between the simulations and the wind tunnel tests for the airflow speed of 12 m s$^{-1}$: 0.082 versus 0.083 deg$^{-1}$ for $k_\alpha$ and 0.084 versus 0.086 deg$^{-1}$ for $k_\beta$. With an angle of attack set to 5°, $k_\beta$ switches by 0.001 deg$^{-1}$ only. The differences in values obtained at 12 and 30 m s$^{-1}$ are not greater than 0.003 deg$^{-1}$. To summarize, the differences between the various estimates do not exceed $\delta_{k\alpha} = 0.001$ deg$^{-1}$ and $\delta_{k\beta} = 0.003$ deg$^{-1}$ for the attack and sideslip coefficients, respectively. The resulting uncertainty $\delta$ on the wind components can therefore be estimated by considering the most significant terms containing $\alpha$ and $\beta$ in the equations:

$$\delta_W \sim \frac{V_a \alpha \delta_{k\alpha}}{k_\alpha} \text{ for the vertical component and}$$

$$\delta_{U,V} \sim \frac{V_a \beta \delta_{k\beta}}{k_\beta} \text{ for the horizontal components.}$$

Taking typical values $V_a = 30$ m s$^{-1}$, $\alpha = 2°$ and $\beta = 2°$, we obtain $\delta_w \sim 0.013$ m s$^{-1}$ and $\delta_{U,V} \sim 0.037$ m s$^{-1}$ (the respective impact on the $U$ and $V$ components being dependent on the angle between the wind direction and the true heading of the UAV). Such orders of magnitude are in the range of the expected precision for wind components.

We checked the validity of these estimates on a real case (the flight presented in section 4), by computing the wind components (according to the equations presented above) first with the values we retained for the coefficients ($k_\alpha = 0.083$ deg$^{-1}$ and $k_\beta = 0.086$ deg$^{-1}$), and then with these values shifted (separately and simultaneously) by their estimated uncertainties ($k_\alpha = 0.082$ deg$^{-1}$ and $k_\beta = 0.083$ deg$^{-1}$). The results are presented in Table 5, and confirm the orders of magnitude we estimated above.

## 4. Experimentation flights and results

### a. Flight patterns and engine operation

In 2018, a qualification flight was conducted. The flight path completed is shown in Fig. 12a. It consisted of a series of

TABLE 4. Calibration coefficients $k_\alpha$ and $k_\beta$ computed from numerical simulations and wind tunnel tests. The coefficients of determination of the regression ($R^2$) are given in parentheses in the last two columns.

| | Air speed (m s$^{-1}$) | Angle of attack (°) | Angle of sideslip (°) | $k_\alpha$ (deg$^{-1}$) | $k_\beta$ (deg$^{-1}$) |
|---|---|---|---|---|---|
| Fluent | 12 | {−10, −5, 5, 10} | 0 | 0.082 (0.9999) | — |
| Fluent | 12 | 0 | {−10, −5, 5, 10} | — | 0.084 (0.9999) |
| Fluent | 12 | 5 | {−10, −5, 5, 10} | — | 0.085 (0.9999) |
| Fluent | 30 | {−10, −5, 5, 10} | 0 | 0.082 (0.9999) | — |
| Fluent | 30 | 0 | {−10, −5, 5, 10} | — | 0.083 (0.9999) |
| Wind tunnel test | 12 | {−10, −5, 5, 10} | 0 | 0.083 (0.9901) | — |
| Wind tunnel test | 12 | 0 | {−10, −5, 5, 10} | — | 0.086 (0.9978) |

TABLE 5. Uncertainties induced on east, north, and vertical wind components due to an error in the calibration factors of angles of attack and sideslip for straight and level runs performed during qualification flight.

| $k_\alpha$, $\delta k_\alpha$ ($\mathrm{deg}^{-1}$) | $k_\beta$, $\delta k_\beta$ ($\mathrm{deg}^{-1}$) | $\delta U$ ($\mathrm{m\ s}^{-1}$) | $\delta V$ ($\mathrm{m\ s}^{-1}$) | $\delta W$ ($\mathrm{m\ s}^{-1}$) |
|---|---|---|---|---|
| (0.083)−0.001 | 0.086 | ±0.001 | ±0.0007 | ±0.016 |
| 0.083 | (0.086)−0.003 | ±0.01 | ±0.03 | ±0.002 |
| (0.083)−0.001 | (0.086)−0.003 | ±0.011 | ±0.031 | ±0.017 |

racetracks at heights between ~500 and ~600 m MSL (the altitude of the ground is around 320 m) (Fig. 12b). The straight branches of the racetrack lasted around 10 s (corresponding to ~300 m), and the total pattern lasted a little less than 1 h.

The analysis of the recorded dataset revealed quite a high level of vibration during some parts of the flight. Without penalizing the measurement of the mean (i.e., averaged over more than 1 s) parameters, these vibrations degrade the quality of turbulence observations, because the high-frequency movements cannot be completely compensated in wind components estimates. A dedicated flight test with seven IMUs with three axis accelerometers, from Digilent company, installed at various locations on the UAV (in the front, the middle, and the rear of the fuselage and in the extremity and middle of the wings), and recorded at a rate of 950 Hz, revealed several peaks at frequencies commensurate with propeller blade rotational speed. Note that due to the limitations in FPGA module pins number, the temperature and humidity module had been replaced by this vibration module. We also found that the level of vibration was highly dependent on the engine speed. An illustration is given in Fig. 13, where it can be clearly seen that the fluctuation in the acceleration mitigates when the engine speed reaches 6000 rpm, which corresponds to an airspeed of around 30 $\mathrm{m\ s}^{-1}$ that is considered as the optimal airspeed at which future flights will be conducted.

We conducted another flight with BOREAL on 4 August 2020. The experiment took place in the atmospheric research center [Centre de Recherche Atmosphérique (CRA)] in Lannemezan (France). This site is equipped among others with a measurement tower of 60-m height (http://p2oa.aero.obs-mip.fr/spip.php?article403) that is instrumented with sonic anemometers on three levels (30, 45, and 60 m). This platform is considered as a reference to our measurements. The flight pattern consisted of back and forth runs at reverse headings as with the 2018 flight. It is represented in Fig. 12c. The

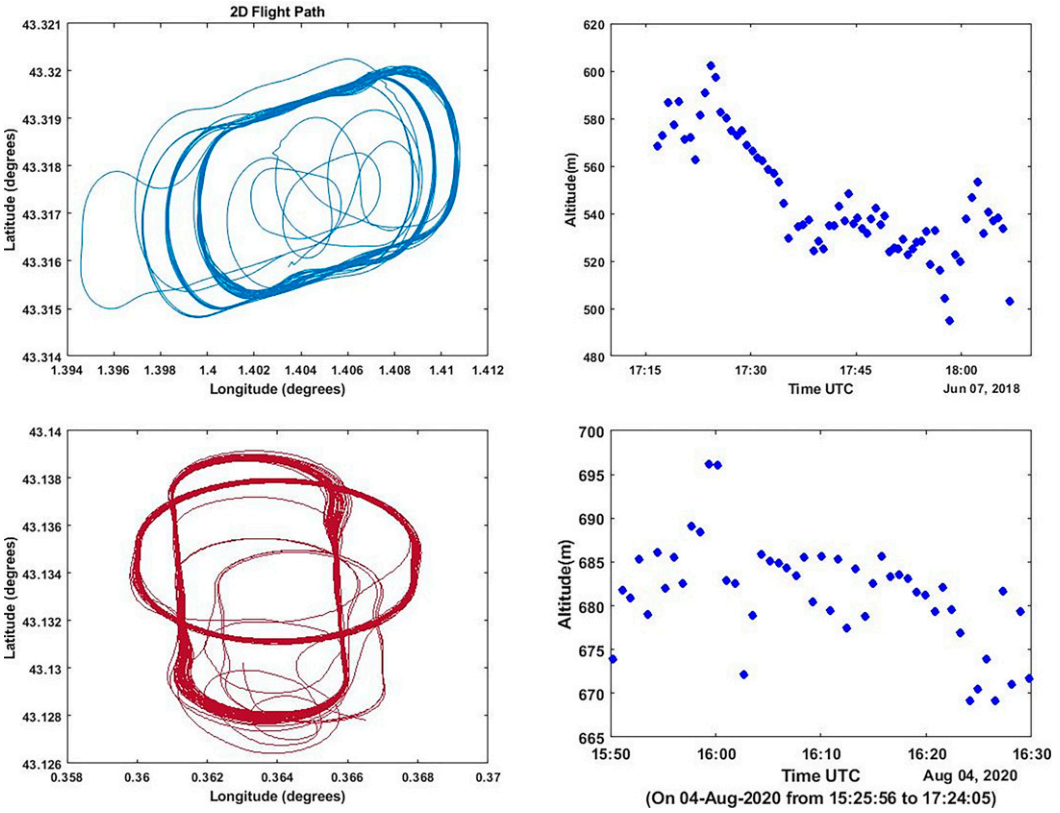


FIG. 12. (top left) Horizontal track and (top right) altitude above sea level of the straight and level runs for the qualification flight on 7 June 2018. (bottom) As in the top row, but for the flight on 4 Aug 2020.

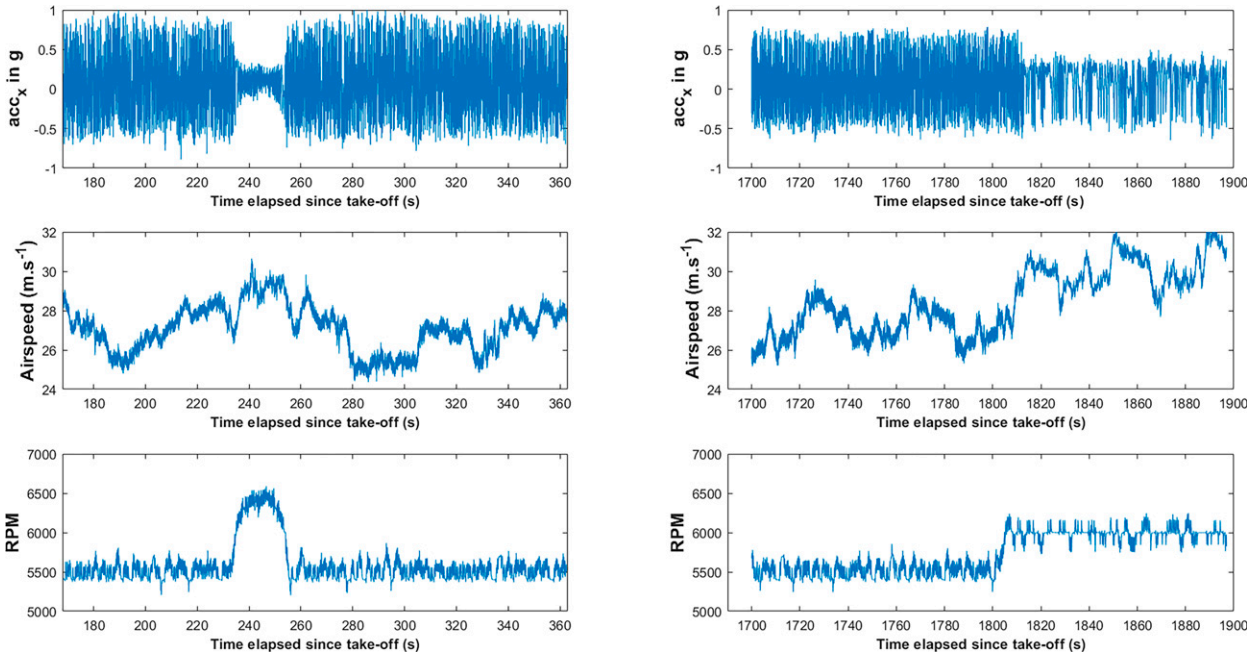


FIG. 13. For the flight of 7 Jun 2018, the columns represent the time series for two different periods of around 3 min each. (top) Acceleration in the longitudinal axis (in g), (middle) true airspeed (in m s$^{-1}$), (bottom) engine speed (rpm).

airspeed was set around 30 m s$^{-1}$, which is the optimal speed at which vibrations are less perceived. The flight altitude was between 670 and 700 m above sea level (see Fig. 12d), i.e., around 80 to 105 m AGL. The center of the pattern is situated a little less than 1 km to the north of the tower. During the flight, the wind was light to moderate coming from the northwest. The aim of this experimental flight is to compare the observations made to those of the 60-m tower.

### *b. Mean wind estimate*

The wind components were computed according to the equations presented in section 2b. The computation to the straight and level branches of the racetrack was restricted, thus excluding the turns during which the estimates are less accurate, due to high values of the roll, varying true airspeeds and unsteady flight conditions. On each branch we computed the mean wind speed and direction, as well as the standard deviations of these parameters.

Since wind direction is a circular variable, the standard deviation was estimated using the method proposed by Yamartino (1984), who proposed the relations

$$\sigma_\theta = \sin^{-1}(\varepsilon)[1 + 0.1547\varepsilon^3],$$

$$\varepsilon^2 = 1 - \left(S_a^2 + C_a^2\right),$$

$$S_a = n^{-1}\sum_i \sin\,\theta_i; \quad C_a = n^{-1}\sum_i \cos\theta_i,$$

where $\sigma_\theta$ is the standard deviation of wind direction and $\theta_i$ is the $i$th value of the computed wind direction series.

Such back and forth runs (reverse headings) are known to be an excellent way through which to evaluate the quality of the wind estimate algorithm. A bias in true airspeed and/or angle of sideslip entails systematic differences in wind estimates on the two run categories. A true airspeed (respectively sideslip) error impacts (at the first order) the wind component on the axis parallel (respectively perpendicular) to the fuselage. An adjustment of the calibrations can therefore be executed by minimizing the wind variation on a pattern like the one performed on this flight. Since the calibrations through numerical simulations and wind tunnel tests cannot be made frequently, adjustments computed from in-flight maneuvers are therefore essential. Such a method, as described by Alaoui-Sosse et al. (2019) was applied to the BOREAL flight. It revealed that no correction was required on the true airspeed, whereas an offset of 2° had to be applied on the angle of sideslip.

For the 2018 flight, the resulting wind speed and wind direction are presented in Fig. 14. The wind is weak to moderate, and presents great variability during the flight, in spite of its rather short duration (less than 1 h), and the narrow height range of the runs (500–600 m AGL). In particular, the computed wind direction switches several times from the west to the east during the flight. To check whether such jumps could be related to a calibration defect that would result in the estimated wind direction turning when the heading was changed, the dots in the figure with two different colors according to the orientation of the racetrack branch were marked. This highlights the fact that the computed wind direction is stable on consecutive runs, the switches between west and east directions occurring at intervals of time much longer than the switch from one branch to another.

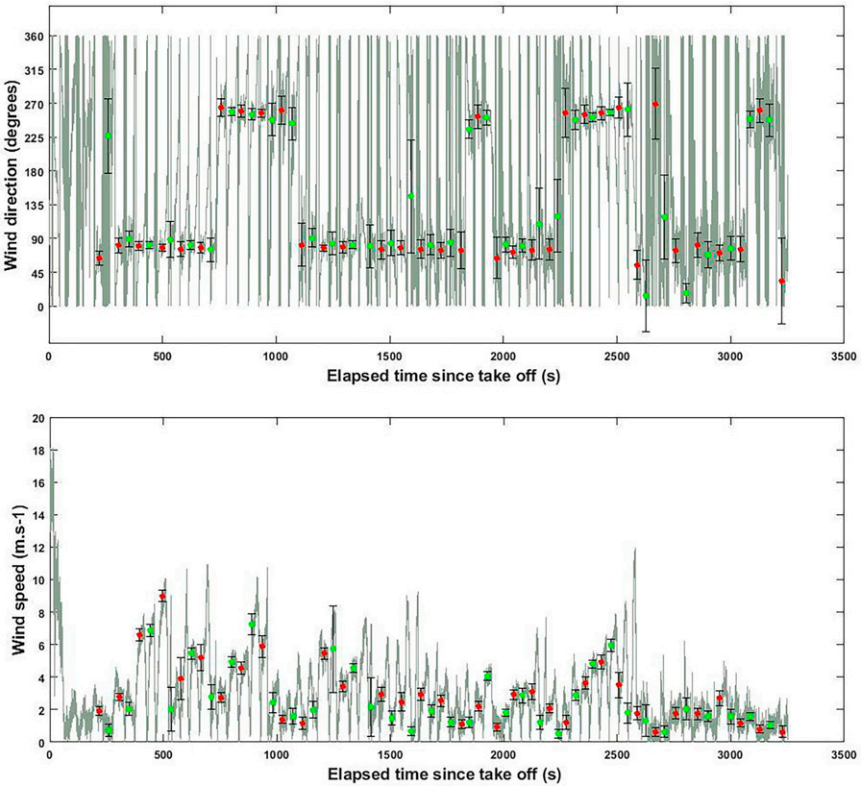


FIG. 14. For the flight of 7 Jun 2018, the time series of the instantaneous (top) wind direction and (bottom) wind speed and their averages over the straight runs of the flight pattern. The error bars represent the standard deviation on each run. The red (green) color refers to the ENE (WSW) flight track.

A possible meteorological origin for this swirling wind was then investigated. Having examined the wind observations on some stations of the French weather service (Météo-France) spread within a few tens of kilometers around the flight area, it was noted that 1) the wind roses in this area are clearly bimodal, with a large majority of winds coming either from E to SE or from W to NW, and 2) the day the flight was performed was characterized by a weak wind with unsteady direction. Unfortunately, the 1-h resolution of the archived data does not allow one to investigate the variability during the flight period.

On the other hand, the 2020 flight allows the comparison of the BOREAL UAV data with those of the 60-m tower, which proves the BOREAL capacity to estimate appropriately the wind vector. For this purpose, the BOREAL data were considered on the straight and level flight sequences and given the flight altitude they were compared to the tower data collected at 60 m. The computation of mean values on the two platforms consists then of selecting the 49 straight runs of the flight and their corresponding periods on the 60-m tower.

The comparison between the 60-m tower and the BOREAL UAV measurements of wind direction and wind speed is illustrated in Fig. 15 where the standard deviations on each run are represented by error bars. Both platforms are coherent regarding mean values. The mean absolute error (MAE) between the 60-m tower and BOREAL UAV of the wind speed is 0.64 m $s^{-1}$ and for wind direction is 12.9°, thus the errors have an order of magnitude included within the acceptable range of the errors targeted with UAVs. The dispersion is slightly higher for BOREAL, which is expected regarding the difficulty of wind estimate with a moving platform. Besides, the observed differences between both platforms results in part from flight altitude, which ranges from 80 to 105 m above ground level. The tower data on the other hand were collected at 60 m, because of the difference in areas sensed by the two platforms since the tower was approximately 1 km from the center of the flight area. Consequently, the coherence between the two systems is considered satisfactory.

### c. Turbulence

In this section, the turbulence observations gathered on 7 June 2018 when the UAV flew with airspeed around 30 m $s^{-1}$ are presented because the vibrations were reduced in such conditions. The three wind components were computed at 100 Hz on the straight and level runs. The corresponding mean spectra (i.e., averaged over several sequences of the same length) are presented in Fig. 16.

The spectra of the three wind components follow the −5/3 power law, characteristic of the inertial subrange, in a

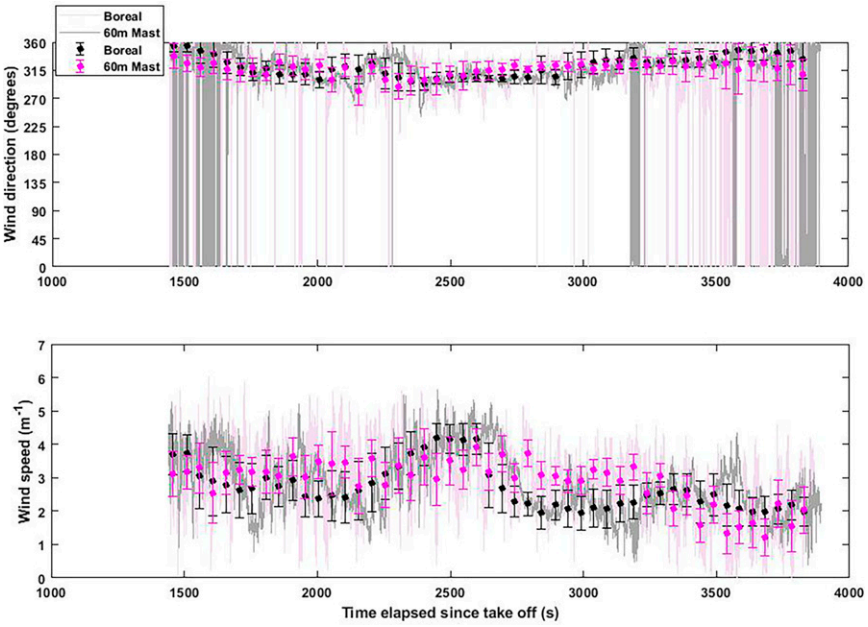


FIG. 15. For the flight of 4 Aug 2020, instantaneous and averaged (top) wind direction and (bottom) wind speed over the straight runs measured by BOREAL (in magenta) and the 60-m tower (in gray and black). The standard deviation corresponding to each straight run is represented by the error bars on the UAV and tower data.

frequency band extending from ~1 to 10 Hz. This latter frequency marks the upper limit to which the turbulence signals can be considered as valid. At higher frequencies, the spectra are spoiled, either by noise (on horizontal components) or by vibration lines (on the vertical one). Quality of the turbulence measurements down to an horizontal resolution of ~3 m can therefore be expected. These results are preliminary but promising. A complete validation, however, will require further flights in various turbulence regimes that can be observed in the boundary layer. Since BOREAL is a heavy UAV, it necessitates for each flight the request of authorizations from the air traffic control authorities. These authorizations are unfortunately not easy to obtain whenever desired and this process takes time. The choice of the weather conditions before each flight test is therefore limited.

## 5. Conclusions

An instrumentation package for wind and turbulence observations in the atmospheric boundary layer embarked in the BOREAL unmanned aerial vehicle has been developed. The platform has the capability to load up to 5 kg of scientific payload and to fly up to 8–9 h. The method used for wind measurements was inspired by what has been performed for several decades on piloted airplanes, and more recently on UAVs (Alaoui-Sosse et al. 2019). It consists of the installation of instrumental devices with the ability to measure all the terms present in the wind equation. Apart from an IMU and a Pitot tube, the nose of the aircraft is replaced by a five-hole hemispherical probe able to measure the angles of attack and sideslip. The calibration of this probe is done using CFD simulations and wind tunnel tests. The calibration coefficients differ slightly from their theoretical value and the estimates were very consistent both from the CFD simulations and the wind tunnel tests. The differences between the two methods, or between various configurations of the flow for a given method, when translated into uncertainties on the wind component estimates, have a negligible impact. In-flight operations revealed that the engine speed must be high enough to reduce vibrations and to allow a good estimate of wind components.

To evaluate the reliability of the mean wind estimates, a flight with numerous back and forth runs at close heights was explored. The passage from a run to the next with a reverse heading did not entail a variation in the wind estimate. Large variations in the computed wind during the flight were, however, observed and attributed to the changing meteorological conditions. The comparison with wind observations on a 60-m tower during a subsequent flight revealed coherence between the two platforms.

The quality of the turbulent wind components was checked through spectra computed on straight and level flight sequences, performed at the appropriate airspeed. The quality of the spectra, evaluated by the $-5/3$ power law in the inertial subrange, is satisfactory up to frequencies of around 10 Hz, which corresponds to a spatial resolution of 3 m. Such a resolution would allow one to capture all the significant turbulent energy in the ABL. Only very close to the surface could the turbulence scales be small enough to significantly contribute to the turbulent kinetic at such frequencies, but given the size of the UAV it cannot be operated below tens of meters. To

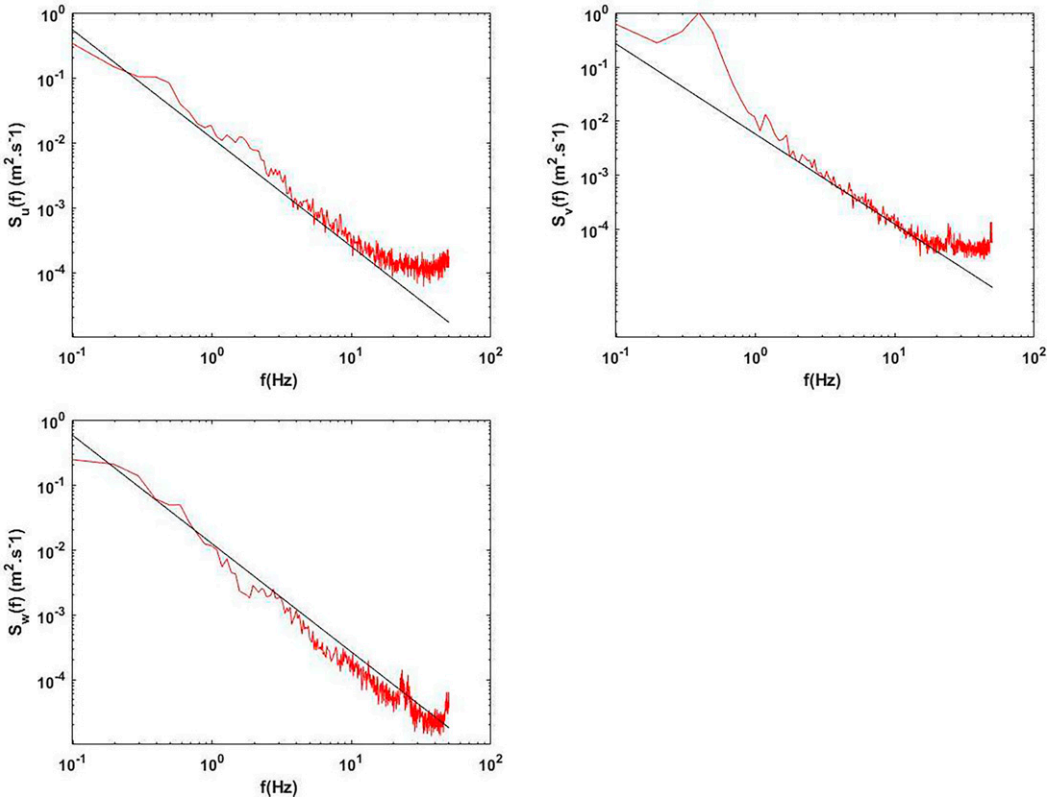


FIG. 16. For the flight of 7 Jun 2018, spectra of (top left) east, (top right) north, and (bottom) vertical wind component computed on straight sequences at a true airspeed of ~30 m $s^{-1}$. The black line on each plot is the −5/3 slope.

complete these promising results, however, we plan to conduct other flights in the future in order to evaluate more comprehensively the performances of BOREAL in terms of measuring turbulence.

In the near future, a completion of the payload with faster temperature and humidity sensors is planned. This will allow the estimation of turbulent fluxes, provided that long-enough straight and level runs could be achieved in spite of flight restrictions. Measurement campaigns will also be conducted in order to compare turbulence estimates on an instrumented tower and a moving platform. One of these campaigns will be devoted to the observation of the wake structure behind wind-turbines.

*Acknowledgments.* This study and the development of the five-hole probe was carried out within the MIRIAD project, which was supported by the regional program FEDER/FSE "Midi-Pyrénées Garonne 2014-2020" "Région Occitanie." BOREAL UAV was purchased in partnership between "Laboratoire d'aérologie," "GET laboratory," and OMP. Observation data on the 60-m tower were collected at the Pyrenean Platform for Observation of the Atmosphere P2OA (http://p2oa.aero.obs-mip.fr). P2OA facilities and staff are funded and supported by the University Paul Sabatier Toulouse 3, France, and Centre National de la Recherche Scientifique (CNRS). We thank ISAE-SUPAERO for financing the Ph.D. thesis of Sara Alaoui-Sosse. We thank as well the EG2R project funded by the RTRA STAE (Toulouse, France), which allowed us to hire Francis Durand and Thomas Le Boulch, who worked on the technical development, and we thank them for their valuable participation to the project. Datasets for this research are not publicly available.

## REFERENCES

Alaoui-Sosse, S., P. Durand, P. Medina, P. Pastor, M. Lothon, and I. Cernov, 2019: OVLI-TA: An unmanned aerial system for measuring profiles and turbulence in the atmospheric boundary layer. *Sensors*, **19**, 581, https://doi.org/10.3390/s19030581.

Altstädter, B., and Coauthors, 2015: ALADINA—An unmanned research aircraft for observing vertical and horizontal distributions of ultrafine particles within the atmospheric boundary layer. *Atmos. Meas. Tech.*, **8**, 1627–1639, https://doi.org/10.5194/amt-8-1627-2015.

Barbieri, L., and Coauthors, 2019: Intercomparison of small unmanned aircraft system (sUAS) measurements for atmospheric science during the LAPSE-RATE campaign. *Sensors*, **19**, 2179, https://doi.org/10.3390/s19092179.

Bärfuss, K., F. Pätzold, B. Altstädter, E. Kathe, S. Nowak, L. Bretschneider, U. Bestmann, and A. Lampert, 2018: New setup of the UAS ALADINA for measuring boundary layer properties, atmospheric particles and solar radiation. *Atmosphere*, **9**, 28, https://doi.org/10.3390/atmos9010028.

Båserud, L., J. Reuder, M. O. Jonassen, S. T. Kral, M. B. Paskyabi, and M. Lothon, 2016: Proof of concept for turbulence measurements with the RPAS SUMO during the BLLAST campaign. *Atmos. Meas. Tech.*, **9**, 4901–4913, https://doi.org/10.5194/amt-9-4901-2016.

——, ——, ——, T. A. Bonin, P. B. Chilson, M. A. Jiménez, and P. Durand, 2020: Potential and limitations in estimating sensible-heat-flux profiles from consecutive temperature profiles using remotely-piloted aircraft systems. *Bound.-Layer Meteor.*, **174**, 145–177, https://doi.org/10.1007/s10546-019-00478-9.

Bonin, T., P. Chilson, B. Zielke, and E. Fedorovich, 2013a: Observations of the early evening boundary-layer transition using a small unmanned aerial system. *Bound.-Layer Meteor.*, **146**, 119–132, https://doi.org/10.1007/s10546-012-9760-3.

——, ——, ——, P. M. Klein, and J. R. Leeman, 2013b: Comparison and application of wind retrieval algorithms for small unmanned aerial systems. *Geosci. Instrum. Methods Data Syst.*, **2**, 177–187, https://doi.org/10.5194/gi-2-177-2013.

Brilouet, P.-E., P. Durand, and G. Canut, 2017: The marine atmospheric boundary layer under strong wind conditions: Organized turbulence structure and flux estimates by airborne measurements. *J. Geophys. Res. Atmos.*, **122**, 2115–2130, https://doi.org/10.1002/2016JD025960.

Brown, E. N., C. A. Friehe, and D. H. Lenschow, 1983: The use of pressure fluctuations on the nose of an aircraft for measuring air motion. *J. Climate Appl. Meteor.*, **22**, 171–180, https://doi.org/10.1175/1520-0450(1983)022<0171:TUOPFO>2.0.CO;2.

Calmer, R., G. Roberts, J. Preissler, S. Derrien, and C. O'Dowd, 2018: Vertical wind velocity measurements using a five-hole probe with remotely piloted aircraft to study aerosol–cloud interactions. *Atmos. Meas. Tech.*, **11**, 2583–2599, https://doi.org/10.5194/amt-11-2583-2018.

Campbell, J. F., and J. M. Brandon, 2011: Calibration and flight results for the Ares I-X 5-hole probe. *Acta Astronaut.*, **68**, 1219–1227, https://doi.org/10.1016/j.actaastro.2010.10.020.

Elston, J. S., 2011: Semi-autonomous small unmanned aircraft systems for sampling tornadic supercell thunderstorms. Ph.D. dissertation, University of Colorado, 293 pp.

——, B. Argrow, M. Stachura, D. Weibel, D. Lawrence, and D. Pope, 2015: Overview of small fixed-wing unmanned aircraft for meteorological sampling. *J. Atmos. Oceanic Technol.*, **32**, 97–115, https://doi.org/10.1175/JTECH-D-13-00236.1.

Houston, A. L., B. Argrow, J. Elston, J. Lahowetz, E. W. Frew, and P. C. Kennedy, 2012: The Collaborative Colorado–Nebraska Unmanned Aircraft System Experiment. *Bull. Amer. Meteor. Soc.*, **93**, 39–54, https://doi.org/10.1175/2011BAMS3073.1.

Lambert, D., and P. Durand, 1998: Aircraft to aircraft intercomparison during SEMAPHORE. *J. Geophys. Res. Oceans*, **103**, 25 109–25 123, https://doi.org/10.1029/97JC02199.

Lawrence, D. A., and B. B. Balsley, 2013: Design of a low-cost UAS for high-resolution atmospheric sensing. *Infotech@Aerospace Conf.*, Boston, MA, AIAA, 4669, https://doi.org/10.2514/6.2013-4669.

Lenschow, D., Ed., 1986a: *Probing the Atmospheric Boundary Layer*. Amer. Meteor. Soc., 269 pp.

——, 1986b: Aircraft measurements in the boundary layer. *Probing the Atmospheric Boundary Layer*, Amer. Meteor. Soc., 39–55.

Mann, J., and D. Lenschow, 1994: Errors in airborne flux measurements. *J. Geophys. Res.*, **99**, 14 519–14 526, https://doi.org/10.1029/94JD00737.

Milanovic, I. M., and I. M. Kalkhoran, 2000: Numerical calibration of a conical five-hole probe for supersonic measurements. *Meas. Sci. Technol.*, **11**, 1812–1818, https://doi.org/10.1088/0957-0233/11/12/322.

Raga, G. B., and S. Abarca, 2007: On the parameterization of turbulent fluxes over the tropical eastern Pacific. *Atmos. Chem. Phys.*, **7**, 635–643, https://doi.org/10.5194/acp-7-635-2007.

Rautenberg, A., M. S. Graf, N. Wildmann, A. Platis, and J. Bange, 2018: Reviewing wind measurement approaches for fixed-wing unmanned aircraft. *Atmosphere*, **9**, 422, https://doi.org/10.3390/atmos9110422.

——, and Coauthors, 2019: The Multi-Purpose Airborne Sensor Carrier MASC-3 for wind and turbulence measurements in the atmospheric boundary layer. *Sensors*, **19**, 2292, https://doi.org/10.3390/s19102292.

Reineman, B. D., L. Lenain, N. M. Statom, and W. K. Melville, 2013: Development and testing of Instrumentation for UAV-based flux measurements within terrestrial and marine atmospheric boundary layers. *J. Atmos. Oceanic Technol.*, **30**, 1295–1319, https://doi.org/10.1175/JTECH-D-12-00176.1.

Reuder, J., P. Brisset, M. M. Jonassen, and S. Mayer, 2009: The Small Unmanned Meteorological Observer SUMO: A new tool for atmospheric boundary layer research. *Meteor. Z.*, **18**, 141–147, https://doi.org/10.1127/0941-2948/2009/0363.

——, L. Båserud, M. O. Jonassen, S. T. Kral, and M. Müller, 2016: Exploring the potential of the RPA system SUMO for multipurpose boundary-layer missions during the BLLAST campaign. *Atmos. Meas. Tech.*, **9**, 2675–2688, https://doi.org/10.5194/amt-9-2675-2016.

Saïd, F., U. Corsmeier, N. Kalthoff, C. Kottmeier, M. Lothon, A. Wieser, T. Hofherr, and P. Perros, 2005: ESCOMPTE experiment: Intercomparison of four aircraft dynamical, thermodynamical, radiation and chemical measurements. *Atmos. Res.*, **74**, 217–252, https://doi.org/10.1016/j.atmosres.2004.06.012.

——, G. Canut, P. Durand, F. Lohou, and M. Lothon, 2010: Seasonal evolution of boundary-layer turbulence measured by aircraft during the AMMA 2006 special observation period. *Quart. J. Roy. Meteor. Soc.*, **136**, 47–65, https://doi.org/10.1002/qj.475.

Tjernström, M., and C. A. Friehe, 1991: Analysis of a radome air-motion system on a twin-jet aircraft for boundary-layer research. *J. Atmos. Oceanic Technol.*, **8**, 19–40, https://doi.org/10.1175/1520-0426(1991)008<0019:AOARAM>2.0.CO;2.

van den Kroonenberg, A., T. Martin, M. Buschmann, J. Bange, and P. Vörsmann, 2008: Measuring the wind vector using the autonomous mini aerial vehicle M2AV. *J. Atmos. Oceanic Technol.*, **25**, 1969–1982, https://doi.org/10.1175/2008JTECHA1114.1.

Wildmann, N., M. Hofsäß, F. Weimer, A. Joos, and J. Bange, 2014a: MASC—A small remotely piloted aircraft (RPA) for wind energy research. *Adv. Sci. Res.*, **11**, 55–61, https://doi.org/10.5194/asr-11-55-2014.

——, S. Ravi, and J. Bange, 2014b: Towards higher accuracy and better frequency response with standard multi-hole probes in turbulence measurement with remotely piloted aircraft (RPA). *Atmos. Meas. Tech.*, **7**, 1027–1041, https://doi.org/10.5194/amt-7-1027-2014.

Witte, B. M., R. F. Singler, and S. C. C. Bailey, 2017: Development of an unmanned aerial vehicle for the measurement of turbulence in the atmospheric boundary layer. *Atmosphere*, **8**, 195, https://doi.org/10.3390/atmos8100195.

Yamartino, R. J., 1984: A comparison of several "single-pass" estimators of the standard deviation of wind direction. *J. Climate Appl. Meteor.*, **23**, 1362–1366, https://doi.org/10.1175/1520-0450(1984)023<1362:ACOSPE>2.0.CO;2.